JOURNAL OF PROPULSION AND POWER
Vol. 24, No. 3, May–June 2008

Loss Mechanisms of High-Turning Supercritical Compressor Cascades

Bo Song*
Gardner Denver, Inc., Peachtree City, Georgia 30269
Wing Ng†
Virginia Polytechnic Institute and State University, Blacksburg, Virginia 24061
Toyotaka Sonoda‡
Honda R&D Co., Ltd., Saitama 351-0193, Japan
and
Toshiyuki Arima§
Honda R&D Co., Ltd., Saitama 351-0193, Japan

DOI: 10.2514/1.30579

This paper presents an experimental and numerical study on loss mechanisms of two high-turning compressor cascades at supercritical flow conditions. It is part of a comprehensive advanced compressor blade development program, in which three cascades were designed at a higher supercritical speed ($M_1 = 0.87$) for a transonic fan stator hub section. The cascades had the same solidity and blade chord but differed significantly in blade profiles. The baseline profile was a conventional controlled diffusion airfoil. The other two were state-of-the-art optimized designs and were experimentally confirmed to outperform the baseline. The first optimized cascade (optimized A) and its performance was published in Song and Ng (Song, B., and Ng, W., "Performance and Flow Characteristics of an Optimized Supercritical Compressor Stator Cascade," *Journal of Turbomachinery*, Vol. 128, July 2006, pp. 435–443). The current paper focuses on comparing the baseline and the second optimized cascade (optimized B) to complement the first publication. Cascade test results are presented to show significant loss reduction (about 30%) from the baseline to the optimized profiles. Experimental and numerical analyses to understand the flow physics underlying the loss reduction are detailed using the following: wake profile, blade surface Mach number, shadowgraph, and blade surface flow visualization. It was found that severe boundary-layer separation occurred in the baseline cascade, whereas the boundary layer of the optimized cascades was well controlled from separation. An understanding of the low-loss flow pattern and design philosophy for high-turning compressor blades at higher supercritical flow conditions, exemplified by the two optimized cascades and relative to the controlled diffusion airfoil, is summarized.

Nomenclature

C	=	blade chord
k	=	turbulent kinetic energy
L	=	blade span
M	=	Mach number
P_s	=	static pressure
P_t	=	total pressure
Re	=	Reynolds number, based on the blade chord and inlet condition
S	=	blade spacing
α	=	flow angle with respect to axial direction
ε	=	isentropic turbulent kinetic energy dissipation rate
γ	=	stagger angle
φ	=	camber angle
ρ	=	density
σ	=	solidity, C/S
ω	=	loss coefficient local or area averaged, $(Pt_1\text{-}Pt_2)/(Pt_1\text{-}Ps_1)$

Subscripts

1	=	inlet plane
2	=	outlet plane
is	=	isentropic

Received 20 February 2007; revision received 11 October 2007; accepted for publication 15 November 2007.

*Senior Product Development Engineer, Engineered Products Division, 100 Gardner Park. Senior Member AIAA.
†Chris Kraft Endowed Professor of Engineering, Department of Mechanical Engineering. Associate Fellow AIAA.
‡Chief Engineer, Aircraft Engine R&D Center, 1-4-1 Chuo, Wako-shi.
§Chief Engineer, Fundamental Technology Research Center, 1-4-1 Chuo, Wako-shi.

I. Introduction

THE compressor development trend of a higher pressure ratio and less weight necessitates reducing the number of stages and increasing the blade loading. Consequently, the flow velocities relative to the blades increased, leading to transonic and supersonic speeds for rotor blades and supercritical flow conditions for stator blades. At supercritical flow conditions, flow in the blade passage accelerates beyond sonic speed although inlet flow remains within the subsonic range. In addition, highly cambered stator blades are needed to generate high flow turning. Therefore, achieving high flow turning at high flow speeds while maintaining low losses turns out to be a great challenge for stator blade design. Hoheisel and Seyb [1] demonstrated that a double circular airfoil (DCA) cascade could only maintain low losses for an inlet Mach number (M_1) up to 0.8, though it was designed at $M_1 = 0.85$ for a flow turning of 50 deg. Hobbs and Weingold [2] confirmed the superiority of the controlled diffusion airfoil (CDA) to the conventional NACA 65 airfoil and the DCA in that the critical inlet Mach number (at which losses increase abruptly) was extended to 0.82. Because of the attractive design concept of shock-free and controlled diffusion without boundary-layer

Table 1 Design condition

M_1	α_1 (Incidence angle)[a], deg	$\Delta\alpha$, deg	AVDR[b]	Diffusion factor[c]	Re[d]
0.87	48.4 (0)	48.4	1.0	0.56	1.5×10^6

[a] $\alpha_1 - \alpha_{1\text{design}}$
[b] $(\rho_2 V_2 \cos\alpha_2)/(\rho_1 V_1 \cos\alpha_1)$
[c] $1 - V_2/V_1 + (V_1 \sin\alpha_1 - V_2 \sin\alpha_2)/(2\sigma V_1)$
[d] Based on the blade chord and inlet condition.

separation, the CDA aroused considerable research interest internationally (Steinert et al. [3], Steinert and Starken [4], Dunker et al. [5], Niederdrenk et al. [6], Sanger [7], Sanger and Shreeve [8], and Elazar and Shreeve [9]). All these works showed the advantage of the CDA at normal supercritical flow conditions ($M_1 \leq 0.82$). In recent years, blade profile optimization drew a lot of attention and seemed promising to improve blade performance [10–14], but verification from test results are rarely seen in the literature. Two advanced subsonic compressor blade development programs have completed verification tests, thus demonstrating the superiority of optimized airfoils [15–18]. It is seen that at more aggressive speeds ($M_1 \geq 0.83$), which can be referred to as "higher supercritical flow conditions," the literature lacks published research on advanced blades, either the CDA or optimized airfoil.

The current research deals with high-turning compressor cascades at higher supercritical flow conditions. The cascade design was for the hub section of a stator in a transonic fan stage of an experimental small turbofan engine, where high flow speed and high tuning were required, as shown in Table 1 (the cascade nomenclature is illustrated in Fig. 1). Targeting this aggressive design condition, three blades were designed independently using different methods. The baseline was a CDA design. The other two were optimized airfoils in an attempt to minimize losses. As shown in Fig. 2, the three blade profiles differ significantly in shape whereas the cascades they compose share a similar setup, as shown in Table 2. The optimized A was obtained using a multi-objective genetic algorithm [19]. The optimized B was generated using an evolution strategy [20]. It is noticed that the baseline CDA has the highest camber at about 30% chord (mostly front cambered) whereas the two optimized blades have the highest camber further downstream at 40–50% chord (mostly midcambered). The optimized A is favored from the mechanical standpoint due to its even thickness distribution control, which was achieved by having thickness control in the optimization process [19].

Cascade testing has demonstrated that both optimized blades exhibit similar performances that are superior to the baseline CDA at higher supercritical flow conditions. Further analysis also indicated similar flow characteristics of the two optimized blades. To focus on a comprehensive presentation of a successfully optimized supercritical cascade, a paper was dedicated to the optimized A [21]. The current paper presents cascade test results and flow analysis of the baseline and optimized B (referred to as "the optimized") in a comparative manner, in an attempt to elucidate the loss reduction mechanisms. As advocated by Denton [22] and reemphasized later by Dunham [23], physical understanding of the flow, particularly the loss mechanisms, is essential for turbomachinery development. The optimized A [21] is referenced when necessary. It is hoped that these two publication efforts will complement each other and enhance the literature on the loss mechanisms of high-turning supercritical compressor cascades.

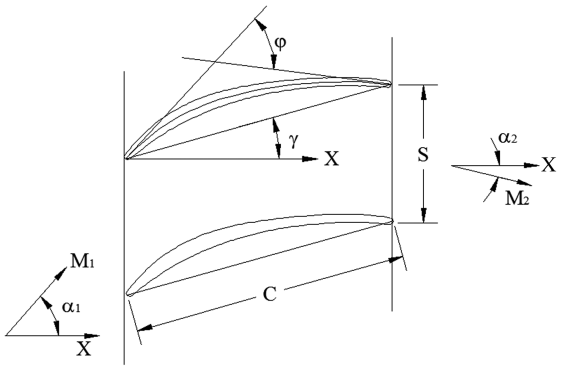

Fig. 1 Cascade nomenclature, where S represents the blade spacing and X is the distance in the axial direction.

II. Facility and Method

Cascade testing was conducted in the Virginia Tech High Speed Cascade Wind Tunnel. The wind tunnel is a blowdown type, with the capacity to sustain high-speed flow for approximately 10 s. High-pressure air, supplied by a four-stage reciprocating compressor, upon discharge from the storage tanks, passed through an activated-aluminum dryer for dehumidification and then proceeded through the inlet section of the tunnel, where a flow straightener and a screen were set to make the flow uniform. Upstream of the test section, a turbulence grid was inserted to increase the inlet flow turbulence level to 1.2–1.6% for the current tests. The flow proceeded to the test section (see Fig. 3). The inlet of the test section had a dimension of 152 mm (width) × 234 mm (height). The fabricated blades to be tested had an aspect ratio of 1.77. A multistage centrifugal blower was used for bottom wall suction to adjust the inlet flow uniformity/periodicity. In addition, a pair of guide vanes and a pair of tailboards were employed to help obtain periodic cascade flow. Solid and slotted sidewalls were used to control the axial velocity density ratio (AVDR).

The temperature was measured upstream of the test section. The cascade was composed of seven blades, numbered 1–7 from the top side to the bottom side. Aerodynamic measurements, as illustrated in Fig. 4, were conducted in the midspan plane. The inlet total pressure was measured 87% blade chord upstream of blade 2 using a total pressure probe. The inlet flow angle was checked 42% chord upstream of the cascade for different pitchwise locations using a three-hole angle probe. Seventeen sidewall pressure taps were evenly spaced in the pitchwise direction 29% chord upstream of the cascade, exactly covering the middle four passages. All of these 17 locations were used to check the inlet flow uniformity/periodicity, whereas some of them were specifically chosen for the inlet Mach number determination. Another three-hole angle probe was traversed 50% chord downstream of the cascade to measure outlet total pressure, Mach number, and flow angle. Overall aerodynamic parameters were area averaged for the middle two passages (from blade 3 to 5). Blade 3 was instrumented on the pressure side whereas blade 4 was instrumented on the suction side for the blade surface pressure measurement. Blade surface flow visualization was performed on the suction surface of blade 4. Shadowgraphs were performed for the passage between blade 3 and 4. Experimental uncertainty is summarized in Table 3. More description of the experimental facility and method was given in Song and Ng [21].

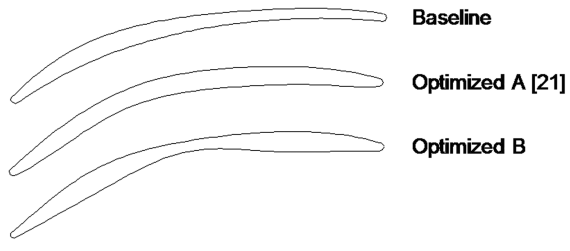

Fig. 2 Blade profile comparison.

Table 2 Cascade geometry

Blade chord		86 mm
Aspect ratio (L/C)		1.77
Solidity (σ)		2
Blade number		7
Stagger angle (γ)	Baseline	15 deg
	Optimized A	16 deg
	Optimized B	16 deg
Camber angle (φ)	Baseline	55 deg
	Optimized A	54 deg
	Optimized B	56 deg
Leading-edge circle radius	Baseline	1.00 mm
	Optimized A	1.00 mm
	Optimized B	0.82 mm

The current paper primarily used the Honda in-house flow solver to analyze the two cascades. It was checked against the flow solver used in Song and Ng [21]. Both solvers rendered similar numerical results except that the solver in Song and Ng [21] overpredicted the separation and losses of the baseline cascade at high speeds. The Honda in-house flow solver computed the blade-to-blade flowfield by solving the two-dimensional, steady, Reynolds-averaged Navier–Stokes equations. The equations were normalized in a generalized curvilinear coordinate system to fit the blade surface. To complete the system of governing equations, the Reynolds stress tensor was evaluated using the Boussinesq eddy viscosity model. To determine values of k and ε, the low Reynolds number formulation of the transport equations for k and ε was also calculated. The governing equations were solved using an implicit time-marching finite-difference scheme to obtain a steady-state solution. The implicit approximately factored scheme, based on the diagonal alternating direction implicit scheme, was used for the time integration. The third-order monotone upstream-centered scheme for conservation laws total variation diminishing formulation with a Van Albada limiter function was applied for the inviscid terms. The viscous terms were evaluated using standard second-order central-difference formulae. To speed up convergence to a steady-state solution, the spatially varying time-stepping technique was employed. More details of this Navier–Stokes solver was given by Arima et al. [24]. Figure 5 shows the computation grid used in the current study. The grid is an H type, compared with an H-O-H grid used in the solver in Song and Ng [21]. The grid size is 221×61.

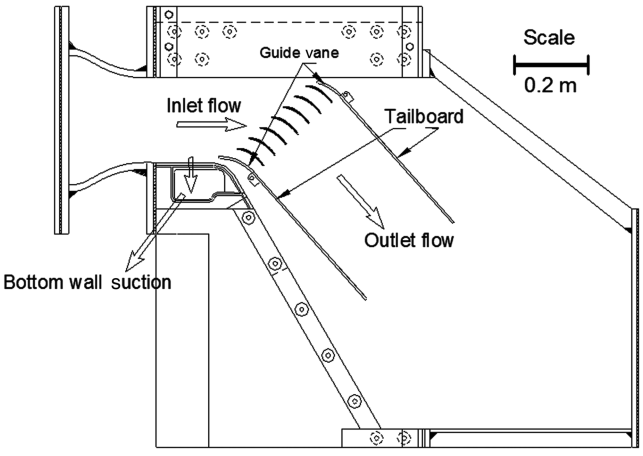

Fig. 3 Cascade test section.

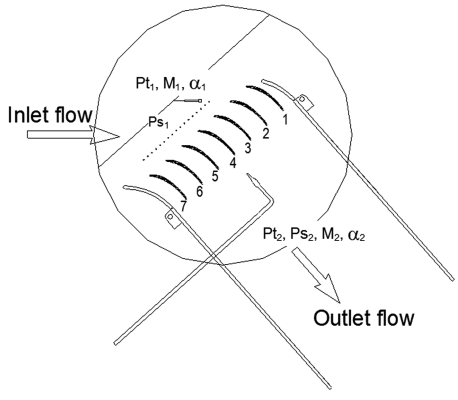

Fig. 4 Aerodynamic measurements.

Table 3 Test conditions and experimental uncertainty

Parameter	Value	Uncertainty
M_1	0.61–0.95	± 0.005
α_1	48.4 deg	± 0.5 deg
AVDR	1.03–1.14	± 0.01
Re	$1.2–1.9 \times 10^6$	$\pm 0.02 \times 10^6$
Freestream turbulence intensity	1.2–1.6%	$\pm 0.05\%$
ω	0.056–0.186	± 0.005

III. Results and Discussion

A. Losses

A full view of the loss performance of the two cascades [based on computational fluid dynamics (CFD)] is shown in Fig. 6. It is seen that the baseline and optimized cascades exhibit similar performances for $M_1 = 0.61$ and 0.78. Low losses are achieved for a wide incidence range for $M_1 = 0.61$ and a moderate incidence range for $M_1 = 0.78$. However, when M_1 was elevated to 0.87, the losses of the baseline cascade dramatically increased whereas the optimized cascade still maintained low losses ($\omega \leq 0.1$) for an incidence range of about 5 deg ($\alpha_1 = 45.4$–50.4 deg). At the design condition ($M_1 = 0.87$, $\alpha_1 = 48.4$ deg), significant loss reduction is obtained. It is seen that loss reduction is also obtained at offdesign incidences at the higher supercritical flow speed. The optimized cascade (optimized B) has very similar loss-incidence characteristics to the optimized A (see Fig. 7 in Song and Ng [21]).

The loss reduction from the baseline to the optimized cascade was confirmed by experiments. Figure 7 shows the measured losses of the two cascades at the design condition at various axial velocity density ratios (AVDR). For all the tested AVDR ranges, significant loss reduction was confirmed. Based on solid sidewall test data, the loss reduction is quantified to be 30%. It is seen that the AVDR variation within the limited range would not affect the relative evaluation of the two cascades. Therefore, the following discussion is based on solid sidewall test results. More discussion of the AVDR effect of these two cascades was given in [25].

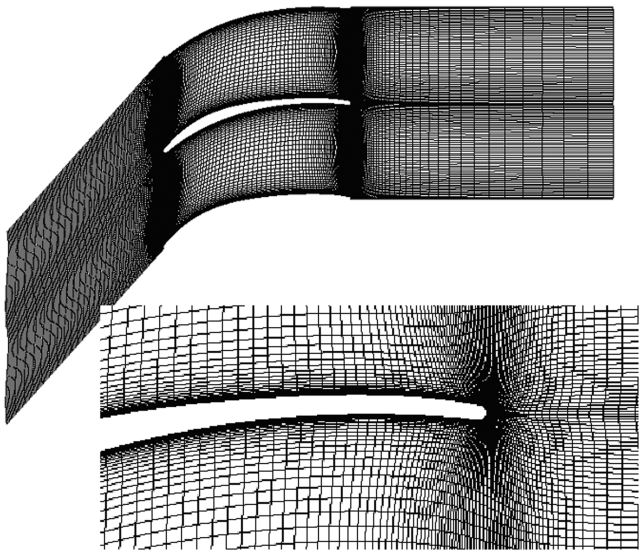

Fig. 5 Computation grid.

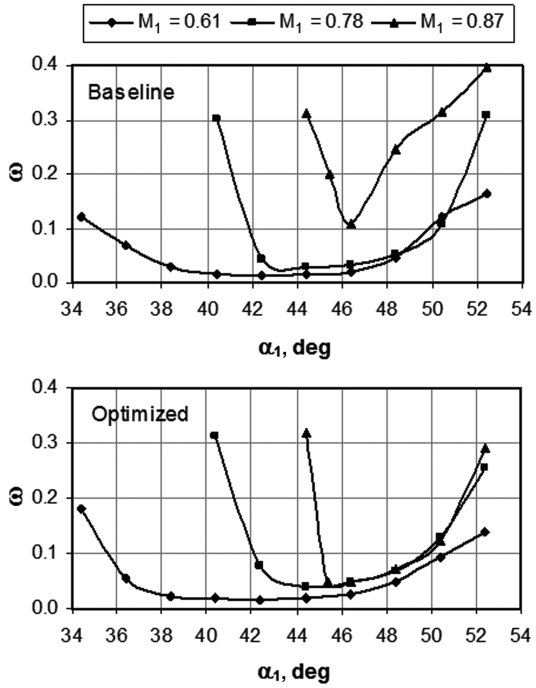

Fig. 6 Computed loss-incidence characteristics.

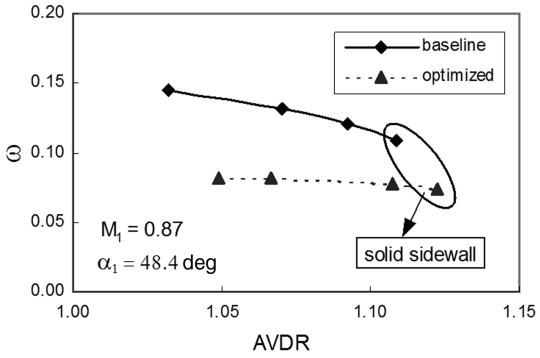

Fig. 7 Measured losses at the design condition with the variation of AVDR.

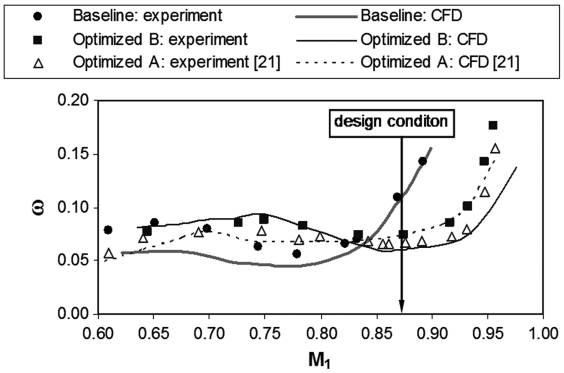

Fig. 8 Loss variation with the inlet Mach number at the design inlet flow angle (48.4 deg).

The loss variation with the inlet Mach number at the design inlet flow angle (48.4 deg) is shown in Fig. 8. Both experimental and CFD results show significant loss reduction from the baseline to the optimized blade (optimized B) at higher supercritical speeds ($M_1 = 0.85$–0.92). The loss-vs-M_1 characteristic of the baseline is typical for a CDA as seen from previous research, that is, the critical inlet Mach number is around 0.83 and, beyond that, losses increase abruptly. In comparison, the optimized blade extends the critical inlet Mach number to 0.91. The optimized blade is demonstrated to have superior performance at higher supercritical flow conditions ($M_1 > 0.83$), including the design condition ($M_1 = 0.87$). For subsonic and normal supercritical speeds ($M_1 = 0.61$–0.83), losses of the optimized blade are higher than the baseline. As the optimization was based on $M_1 = 0.87$ without addressing lower speeds, the tradeoff seen here should not be a surprise. The inferiority of the optimized blade to the baseline at lower M_1 shown by experimental results is not as significant as indicated by the CFD prediction. For reference, the optimized A [21] is included in the figure. Experimental results indicate that the two optimized cascades exhibit very similar loss characteristics and that the optimized A performs slightly better than the optimized B. The discrepancy of the CFD results is due to different flow solvers and AVDR effects. Nonetheless, the CFD prediction is adequate to differentiate the baseline and optimized blades.

B. Flow Mechanisms for Loss Reduction

1. Flow Behavior at the Design Condition

Downstream traverse measurements of the total pressure loss distribution at the design condition are shown in Fig. 9. The baseline has wider and deeper wakes, contributing to its higher loss level than the optimized cascade as seen in Fig. 8. There is a "small hump" in the core flow of the optimized cascade, which will be discussed later. Although the small hump causes higher losses in the core flow, the optimized cascade has a much smaller wake size and thus much lower overall losses than the baseline.

Blade boundary-layer behavior was investigated using blade surface oil flow visualization. The suction surfaces were coated with a thin layer of oil in which a finely powdered color pigment was dissolved. When the tunnel was turned on, the colored oil film was carried with the surface flow such that the flow direction on the blade surface was visualized. After the tunnel run, the streaky oil pattern left on the blade was photographed. A picture of the flow visualization is shown in Fig. 10. Reverse flow was observed on the suction surface of the baseline blade during the tunnel run, confirming the boundary-layer separation. Separation started around 20% chord and did not reattach. In contrast, the optimized blade was observed to have attached flow all along the blade until the trailing edge.

Figure 11 shows the 2-D CFD Mach number contours at the design condition. A typical supersonic patch for supercritical blades is seen at the front part of each blade on the suction side, terminated by a passage shock at 20% chord. The baseline blade has the flow acceleration around the leading edge and, after a short deceleration, reaccelerates to a higher velocity. The higher velocity region ends at the shock location. After the shock, where the blade is highly cambered, the boundary layer separates. The optimized blade, however, has the highest velocity occurring around the leading edge, resulting in a leading-edge shock. After that, the flow decelerates to the passage shock location. The leading-edge shock hits the passage shock, seen as two dark stripes that form a "λ" shape. The shock patterns are better exhibited by shadowgraphs (Fig. 12). CFD and

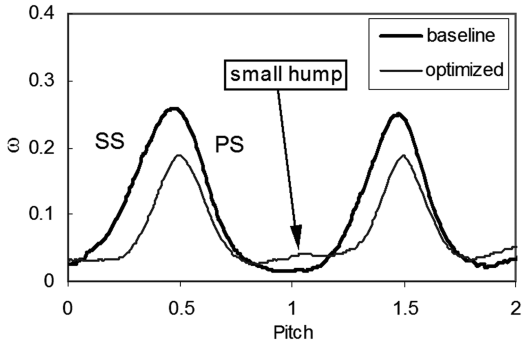

Fig. 9 Measured wake profiles at the design condition ($M_1 = 0.87$, $\alpha_1 = 48.4$ deg, 50% blade chord downstream), where SS is the suction surface and PS is the pressure surface.

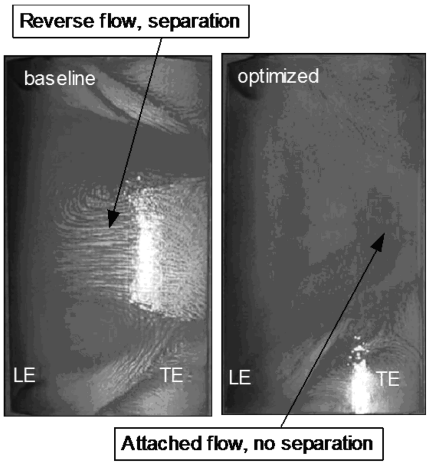

Fig. 10 Blade suction surface flow visualization at the design condition ($M_1 = 0.87, \alpha_1 = 48.4$ deg), where LE is the leading edge and TE is the trailing edge.

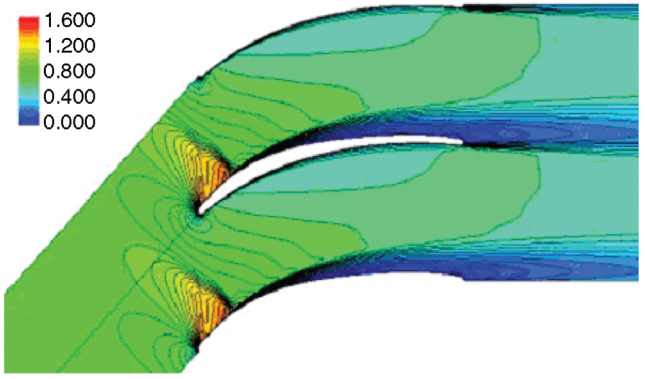

a) Baseline

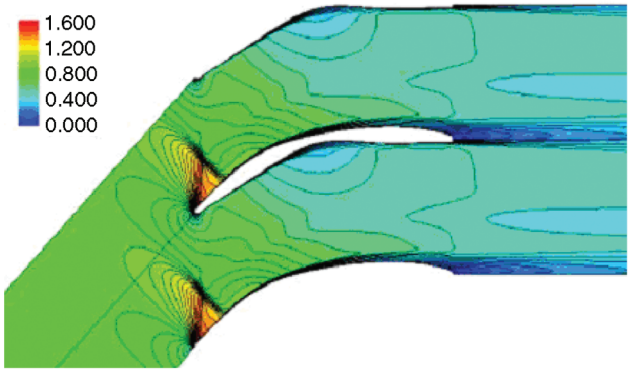

b) Optimized

Fig. 11 2-D CFD Mach number contours at the design condition ($M_1 = 0.87, \alpha_1 = 48.4$ deg,).

experiment shadowgraphs captured the same shock shapes: the passage shock of the baseline blade is a little bowed whereas the passage shock of the optimized blade is straight. Figures 11 and 12 also show different shock strength distribution for the two cascades: the shock of the baseline is stronger near the blade surface and becomes mitigated when it penetrates into the core flow; the optimized has the strongest shock in the core flow, away from the blade surface. Moreover, the optimized blade is less cambered in the shock position. As such, no boundary-layer separation occurred on the optimized blade.

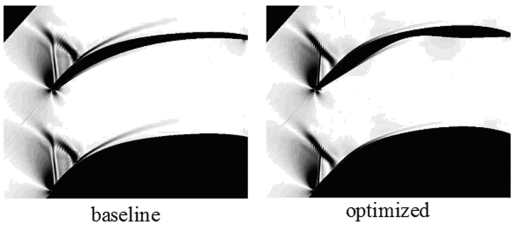

a) CFD

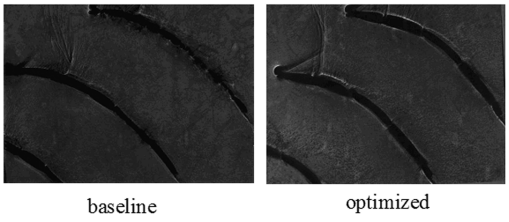

b) Experiment

Fig. 12 Shadowgraphs at the design condition ($M_1 = 0.87$, $\alpha_1 = 48.4$ deg,).

2. Blade Surface Mach Number

The loss-vs-M_1 characteristics shown in Fig. 8 are now interpreted using blade surface isentropic Mach number results (see Figs. 13 and 14). CFD results agree with experimental results at the front part of each blade. After 20% chord, CFD values are lower than the experimental data due to the AVDR influence [25]. The CFD and experiment show similar shapes of the loading envelope. As seen in Fig. 13a, the baseline blade has the desired CDA performance at $M_1 = 0.75$, that is, continuous diffusion along the entire suction surface without boundary-layer separation and a nearly constant subsonic Mach number on the pressure surface. This Mach number distribution trend looks similar to that of Elazar and Shreeve [9]. It is different from the typical trend [2] as there is no continuous acceleration from the leading edge up to 20% chord, referred to as the "ski-jump" [26]. Cumpsty and Dong questioned Elazar and Shreeve about the difference [9]. Test results at other incidences by the current research indicated that it was the incidence that changed the surface Mach number distribution trend. As shown in Fig. 15, the typical CDA blade surface Mach number distribution [2] was found at the inlet flow angle 45.4 deg on the baseline blade.

Increasing M_1 to 0.84–0.90 (Figs. 13b–13d) for the baseline blade, the velocity pattern changes essentially as follows: the leading-edge peak velocity lowers, followed by acceleration to a second velocity peak (around 20% chord). Right after the second peak, signs of the passage shock and the subsequent boundary-layer separation can be recognized. As M_1 increases from 0.84 to 0.90, the second acceleration becomes stronger, resulting in a stronger passage shock and boundary-layer separation, so that losses increase remarkably (see Fig. 8).

As seen from Fig. 14, the flow behavior of the optimized blade differs considerably from the baseline blade. First, the velocity varies significantly on the pressure surface of the optimized blade, with a big depression around midchord, resulting in more even loading distribution compared with the front loading of the baseline blade. Second, stronger leading-edge acceleration is present, generating a strong leading-edge shock, such that the onset of the second acceleration is delayed to higher inlet Mach numbers (Figs. 14c and 14d). At the design point ($M_1 = 0.87$, Fig. 14b), the deceleration lasts from the leading edge to the passage shock (around 20% axial chord) and no apparent velocity peak can be observed. Recall that no boundary-layer separation occurred at this condition as discussed earlier. Even when M_1 increased to 0.91, the second velocity peak is not as distinct as that of the baseline blade at $M_1 = 0.87$ (compare Figs. 13c and 14c). No sign of boundary-layer separation after the second velocity peak is suggested by Fig. 14c either. When M_1 further increased to 0.95, the velocity pattern at the front part of the suction surface becomes similar to that of the baseline at $M_1 = 0.87$, with the passage shock occurring further downstream than the

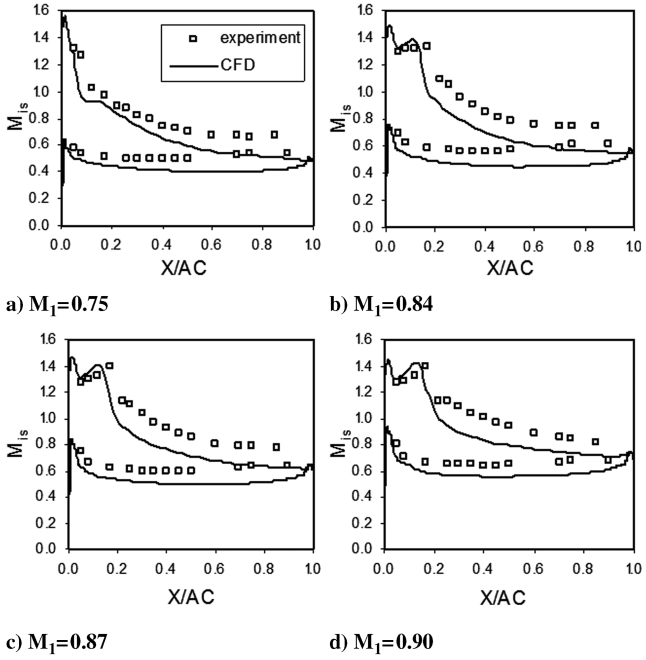

Fig. 13 Baseline blade surface isentropic Mach number at the design inlet flow angle (48.4 deg), where X is the distance in the axial direction and AC is the axial chord.

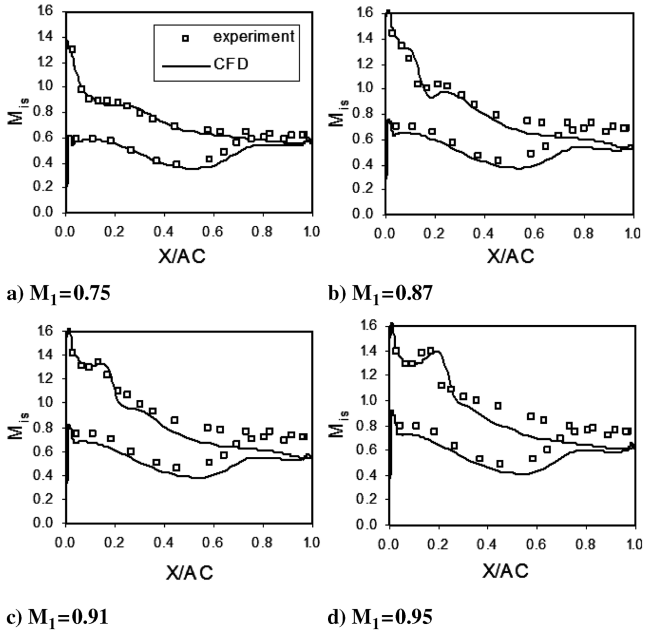

Fig. 14 Optimized blade surface isentropic Mach number at the design inlet flow angle (48.4 deg), where X is the distance in the axial direction and AC is the axial chord.

baseline. At $M_1 = 0.95$, the passage shock of the optimized blade is strong enough to initiate boundary-layer separation, thus losses increase abruptly (See Fig. 8).

It is worth pointing out that the optimized A [21], though it was generated independently and had a different shape, exhibited similar blade surface Mach number distribution characteristics as the current optimized B. The more even blade loading distribution of the two optimized blades relative to the front loading of the baseline CDA, which benefits boundary-layer separation control and low losses at higher supercritical speeds, is probably due to their common feature: they are highly midchord cambered.

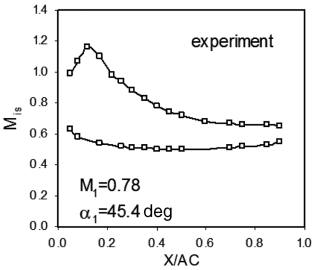

Fig. 15 Typical CDA surface Mach number distribution seen on the baseline blade (45.4 deg), where X is the distance in the axial direction and AC is the axial chord.

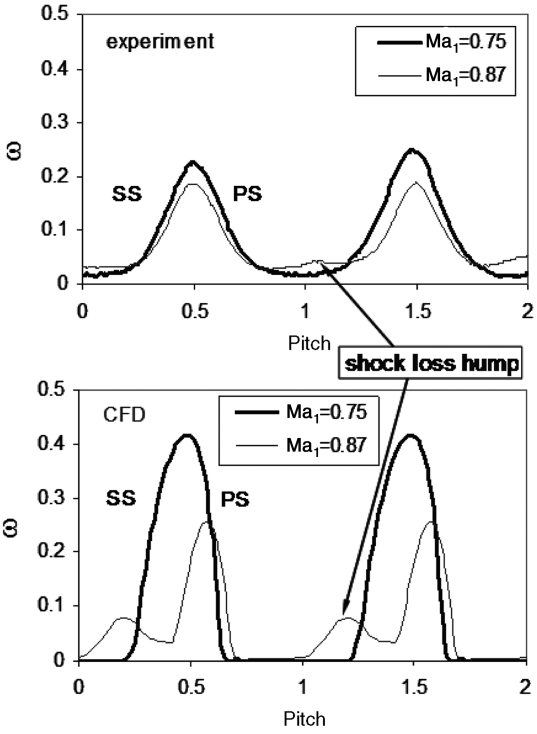

Fig. 16 Wake profiles of the optimized blade at the design inlet flow angle (48.4 deg, 50% blade chord downstream).

C. Double-Peak Wake Profile

The phenomenon of the aforementioned small hump in the wake profile of the optimized blade, or "double-peak wake profile" (see Fig. 9), is explained below. Figure 16 gives the comparison of the wake profiles at $M_1 = 0.75$ and 0.87. The CFD captured this double-peak wake pattern. Probably due to underprediction of the flow mix out process (the CFD and experimental wake profiles were obtained at the same exit location), the CFD shows a deeper and narrower wake and more distinct small hump. Nonetheless, both the experiment and CFD reveal the same flow structure: the leading-edge shock hits the passage shock (see Fig. 12), resulting in local high losses. The high-loss flow is transported downstream, and captured as the small hump. Figure 17 shows the high-loss contour in the passage. This kind of double-peak wake profile was also reported by Kunz and Lakshminarayana [27] in a supersonic compressor cascade.

As shown in Fig. 17, the decrease of the overall losses when increasing M_1 from 0.75 to 0.87 is due to a change in the boundary-layer characteristic. Boundary-layer separation occurs at $M_1 = 0.75$ whereas flow remains attached at $M_1 = 0.87$. The understanding may come from Figs. 14a, 14b, and 18. At $M_1 = 0.75$, flow decelerates abruptly right after the leading edge (no. 1) with the passage shock very close to the leading edge (no. 2). Both factors (no. 1 and 2) conjointly make a strong adverse pressure gradient (see

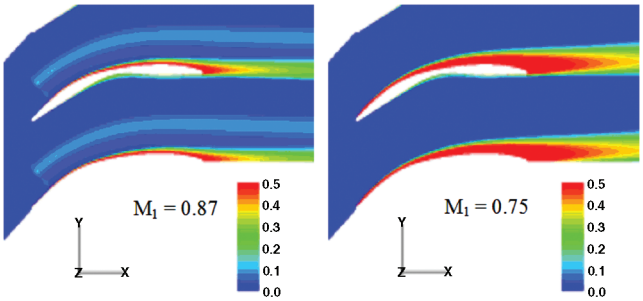

Fig. 17 CFD contours of the loss coefficient of the optimized blade at the design inlet flow angle (48.4 deg).

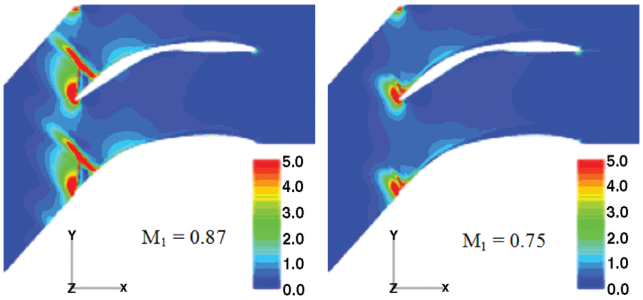

Fig. 18 CFD contours of the normalized pressure gradient of the optimized blade at the design inlet flow angle (48.4 deg).

Fig. 14a), causing mild boundary-layer separation. When M_1 increased to 0.87, the passage shock moves further downstream and the factors (no. 1 and 2) are separated spatially, making a two-step deceleration, and the shock is followed by a reacceleration (favorable pressure gradient) (see Fig. 14b). As such, no separation occurs at $M_1 = 0.87$.

This discussion suggests that the double-shock phenomenon occurring on the optimized blade is a favorable flow structure for low overall losses at higher supercritical speeds like $M_1 = 0.87$. At normal supercritical speeds like $M_1 = 0.75$, the optimized blade sacrificed performance to some degree, whereas the conventional CDA blade excels (see Fig. 8). Referring to the favorable flow structure seen on the optimized A [21], whose leading-edge shock is not strong enough to cause the double-peak wake phenomenon, some general understanding on the low-loss flow structure of high-turning compressor cascades at higher supercritical flow conditions can be obtained:

1) An advantageous velocity development in the blade passage is needed: leading edge acceleration → deceleration → shock → re-acceleration → final diffusion. For the cascade to fulfill high diffusion and high turning of the flow, the process of overcoming the total adverse pressure gradient needs to be fulfilled in this step-by-step sequence.

2) The multishock pattern as exhibited by the optimized A [21] seems to fit the preceding philosophy well.

3) The double-peak wake as exhibited by the optimized B is not essential for maintaining the low-loss mechanism but strong leading-edge acceleration seems necessary.

4) Although different blade shapes can be obtained from independent optimization designs that qualify the low-loss philosophy, a high midchord camber seems to be a common feature.

5) The conventional CDA concept with blades being highly front cambered does not qualify the low-loss philosophy found in the current study, as the strong passage shock coincides with the high camber where the boundary layer cannot sustain from separation.

IV. Conclusions

Cascade testing confirmed that significant loss reduction was obtained from the baseline CDA to the optimized blade at higher supercritical speeds ($M_1 > 0.83$). The baseline blade has significantly elevated losses when the inlet Mach number is raised to higher supercritical speeds due to severe boundary-layer separation on the blade suction surface. The optimized blade maintains low losses up to a much higher speed ($M_1 = 0.91$) due to a well-controlled boundary layer without separation, despite the presence of shocks. Because of the interaction of the leading-edge shock and the passage shock, a local high-loss region is formed in the core flow, resulting in a double-peak wake profile (small hump) downstream of the cascade.

Advanced compressor stator blades are designed for high turning and high speeds with the requirement of low losses. At higher supercritical flow conditions, shocks seem unavoidable. The conventional CDA, though it excels at normal supercritical flow conditions ($M_1 < 0.8$), does not qualify the low-loss design as its shock-free criterion is no longer met at higher speeds. As showcased by the optimized blades, the low-loss design philosophy is to control the shock–boundary-layer interaction and set a favorable velocity development pattern. The overall losses are mostly affected by whether or not the boundary layer separates, with a secondary contribution from shock loss. A favorable flow pattern should start with strong leading-edge acceleration, then deceleration to the passage shock, reacceleration after the shock, then high blade camber, and final diffusion toward the trailing edge. As such, the flow can overcome the adverse pressure gradient progressively and avoid separation. Although different blade shapes can be obtained by different optimization methods to qualify the low-loss design, high midchord camber seems to be a commonly desired feature.

Acknowledgments

The authors gratefully acknowledge Honda R&D Co., Ltd., for sponsoring the research and giving permission to publish the results. The help from Shiming Li, Xingmin Gui, and Hans Raven in the experiments is greatly appreciated. Thanks to the reviewers and the editor for their constructive comments to improve the paper.

References

[1] Hoheisel, H., and Seyb, N. J., "The Boundary Layer Behavior of Highly Loaded Compressor Cascade at Transonic Flow Conditions," *Transonic and Supersonic Phenomena in Turbomachines*, CP-401, AGARD, 1987, pp. 4.1–4.17.

[2] Hobbs, D. E., and Weingold, H. D., "Development of Controlled Diffusion Airfoils for Multistage Compressor Application," *Journal of Engineering for Gas Turbines and Power*, Vol. 106, April 1984, pp. 271–278.

[3] Steinert, W., Eisenberg, B., and Starken, H., "Design and Testing of a Controlled Diffusion Airfoil Cascade for Industrial Axial Flow Compressor Application," *Journal of Turbomachinery*, Vol. 113, Oct. 1991, pp. 583–590.

[4] Steinert, W., and Starken, H., "Off-Design Transition and Separation Behavior of a CDA Cascade," ASME Paper 94-GT-214, 1994.

[5] Dunker, R., Rechter, H., Starken, H., and Weyer, H., "Redesign and Performance Analysis of a Transonic Axial Compressor Stator and Equivalent Plane Cascades with Subsonic Controlled Diffusion Blades," *Journal of Engineering for Gas Turbines and Power*, Vol. 106, April 1984, pp. 279–287.

[6] Niederdrenk, P., Sobieczky, H., and Dulikravich, G. S., "Supercritical Cascade Flow Analysis with Shock-Boundary Layer Interaction and Shock-Free Redesign," *Journal of Turbomachinery*, Vol. 109, July 1987, pp. 413–419.

[7] Sanger, N. L., "The Use of Optimization Techniques to Design Controlled-Diffusion Compressor Blading," *Journal of Engineering for Power*, Vol. 105, April 1983, pp. 256–264.

[8] Sanger, N. L., and Shreeve, R. P., "Comparison of Calculated and Experimental Cascade Performance for Controlled-Diffusion Compressor Stator Blading," *Journal of Turbomachinery*, Vol. 108, July 1986, pp. 42–50.

[9] Elazar, Y., and Shreeve, R. P., "Viscous Flow in a Controlled Diffusion Compressor Cascade with Increasing Incidence," *Journal of Turbomachinery*, Vol. 112, April 1990, pp. 256–266.

[10] Benini, E., and Toffolo, A., "Development of High-Performance Airfoils for Axial Flow Compressors Using Evolutionary Computation," *Journal of Propulsion and Power*, Vol. 18, No. 3, 2002, pp. 544–554.

[11] Oksuz, O., Akmandor, I., and Kavsaoglu, M., "Aerodynamic Optimization of Turbomachinery Cascades Using Euler/Boundary-Layer Coupled Genetic Algorithms," *Journal of Propulsion and Power*, Vol. 18, No. 3, 2002, pp. 652–657.

[12] Rai, M., and Madavan, N., "Application of Artificial Neural Networks to Design of Turbomachinery Airfoils," *Journal of Propulsion and Power*, Vol. 17, No. 1, 2001, pp. 176–183.

[13] Yiu, K. F. C., and Zangeneh, M., "Three-Dimensional Automatic Optimization Method for Turbomachinery Blade Design," *Journal of Propulsion and Power*, Vol. 16, No. 6, 2000, pp. 1174–1181.

[14] Choo, B., and Zangeneh, M., "Development of an (Adaptive) Unstructured 2-D Inverse Design method for Turbomachinery Blades," American Society of Mechanical Engineers Paper GT-2002-30620, 2002.

[15] Köller, U., Mönig, R., Küsters, B., and Schreiber, H., "Development of Advanced Compressor Airfoils for Heavy-Duty Gas Turbines—Part 1: Design and Optimization," *Journal of Turbomachinery*, Vol. 122, July 2000, pp. 397–405. doi:10.1115/1.1302296

[16] Küsters, B., Schreiber, H., Köller, U., and Mönig, R., "Development of Advanced Compressor Airfoils for Heavy-Duty Gas Turbines—Part 2: Experimental and Theoretical Analysis," *Journal of Turbomachinery*, Vol. 122, July 2000, pp. 406–415. doi:10.1115/1.1302321

[17] Sonoda, T., Yamaguchi, Y., Arima, T., Olhofer, M., Sendhoff, B., and Schreiber, H., "Advanced High Turning Compressor Airfoils for Low Reynolds Number Condition—Part 1: Design and Optimization," *Journal of Turbomachinery*, Vol. 126, No. 3, 2004, pp. 350–359. doi:10.1115/1.1737780

[18] Schreiber, H., Steinert, W., Sonoda, T., and Arima, T., "Advanced High Turning Compressor Airfoils for Low Reynolds Number Condition—Part 2: Experimental and Numerical Analysis," *Journal of Turbomachinery*, Vol. 126, No. 4, 2004, pp. 482–492. doi:10.1115/1.1737781

[19] Yamaguchi, Y., and Arima, T., "Multi-Objective Optimization for the Transonic Compressor Stator Blade," AIAA Paper 2000-4909, 2000.

[20] Olhofer, M., Arima, T., Sonoda, T., and Sendhoff, B., "Optimization of a Stator Blade used in a Transonic Compressor Cascade with Evolution Strategies," *Adaptive Computation in Design and Manufacture*, edited by I. Parmee, Springer–Verlag, Berlin/New York/Heidelberg, 2000, pp. 45–54.

[21] Song, B., and Ng, W., "Performance and Flow Characteristics of an Optimized Supercritical Compressor Stator Cascade," *Journal of Turbomachinery*, Vol. 128, July 2006, pp. 435–443. doi:10.1115/1.2183316

[22] Denton, J. D., "Loss Mechanism in Turbomachines," *Journal of Turbomachinery*, Vol. 115, Oct. 1993, pp. 621–656.

[23] Dunham, J., "Aerodynamic Losses in Turbomachines," *Loss Mechanism and Unsteady Flows in Turbomachines*, CP-571, AGARD, 1996, pp. K1–K13.

[24] Arima, T., Sonoda, T., Shirotori, M., Tamura, A., and Kikuchi, K., "A Numerical Investigation of Transonic Axial Compressor Rotor Flow Using a Low-Reynolds Number k–ε Turbulence Model," *Journal of Turbomachinery*, Vol. 121, Jan. 1999, pp. 44–58.

[25] Song, B., and Ng, W., "Influence of Axial Velocity Density Ratio in Cascade Testing of Supercritical Compressor Blades," AIAA Paper 2004-3414, 2004.

[26] Cumpsty, N. A., *Compressor aerodynamics*, Longman Scientific & Technical, Essex, England, U.K., 1989.

[27] Kunz, R. F., and Lakshminarayana, B., "Explicit Navier–Stokes Computation of Cascade Flows Using the κ–ε Turbulence Model," *AIAA Journal*, Vol. 30, No. 1, 1992, pp. 13–22.

A. Prasad
Associate Editor